Dalton Transactions

ROYAL SOCIETY OF CHEMISTRY

PAPER

View Article Online
View Journal | View Issue

Cite this: *Dalton Trans.*, 2020, **49**, 12458

Magnetic field and dilution effects on the slow relaxation of {Er_3} triangle-based arsenotungstate single-molecule magnets†

Hanhan Chen,[a] Lin Sun,[a] Jinpeng Zhang,[a] Zikang Xiao,[a] Pengtao Ma, *[a] Jingping Wang, [a] Yiquan Zhang *[b] and Jingyang Niu *[a]

Received 21st May 2020,
Accepted 23rd July 2020

DOI: 10.1039/d0dt01831g

rsc.li/dalton

A triangular {Er_3} cluster containing polyoxometalate (POM), $[Er_3(\mu_3\text{-}OH)(H_2O)_8(AsW_9O_{33})(AsW_{10}O_{35}(DL\text{-}mal))]_2^{22-}$ (**1**) (mal = malate), has been obtained *via* one-pot reactions. Structural analyses demonstrate that three Er^{3+} ions bridged one μ_3-OH to generate a rare μ_3-OH-capped triangular {Er_3} cluster, which connects two different vacant polyanions to form an unsymmetrical sandwich-type subunit, and adjacent sandwiched subunits are linked through mal ligands to give the targeted dimer. When the Er^{3+} ions are substituted in whole or in part with Y^{3+} ions, the diamagnetic yttrium analogue $[Y_3(\mu_3\text{-}OH)(H_2O)_8(AsW_9O_{33})(AsW_{10}O_{35}(DL\text{-}mal))]_2^{22-}$ (**2**) and diluted sample $[Er_{0.15}Y_{2.85}(\mu_3\text{-}OH)(H_2O)_8(AsW_9O_{33})(AsW_{10}O_{35}(DL\text{-}mal))]_2^{22-}$ (**Er@2**) have also been synthesized. Magnetic studies reveal that **1** exhibits field-induced two-step magnetic relaxation processes; the slow relaxation process may arise from intramolecular magnetic interactions, whereas the fast one is likely to originate from the intermolecular dipole–dipole interactions supported by the magnetic results of **Er@2**. From *ab initio* calculations, it is found that although the magnetic anisotropies of **1** mainly originate from individual Er^{3+} fragments, the Er^{3+}–Er^{3+} interactions have a considerable influence on their slow magnetic relaxation processes.

Introduction

Polyoxometalates (POMs) are generally composed of W, Mo, V, Nb, and Ta in their highest oxidation states, bridged by oxygen atoms to form clusters, which can range in size from low-nuclearity building blocks to large-scale protein-like superstructures.[1,2] Because of the large structural diversity and significant applications in many fields such as catalysis, molecular magnetism, and materials science, ensuring the design and preparation of novel POMs is an attractive and challenging project.[3–5] Moreover, POMs as one unique type of inorganic ligand, possessing a remarkable degree of molecular and electronic tunability, have provided excellent examples for molecular magnets, especially for single-molecule magnets (SMMs).[6] However, lanthanide (Ln) ions usually have large magnetic moments and appreciable magnetic anisotropy, springing from the intense spin–orbit coupling in low-symmetry crystal fields, therefore making them excellent candidates for the construction of SMMs.[7]

The pioneering works on POMs-based molecular magnetism have been promoted by Coronado's group;[8] they summarized the molecular magnetism of POMs for the first time in 1995,[8a] and they systematically reviewed the transition metal magnetic clusters encapsulated by polyoxotungstate and the mixed-valence POM-based magnetic clusters in 1999.[8b] Recent studies indicate that the employment of lacunary POMs to assemble with Ln ions may be an effective strategy to harvest compounds with novel electronic and magnetic behavior.[9] As a result, a large number of Ln-based POMs (Ln-POMs) have been extensively developed,[6–9] especially Dy-containing POMs with SMM behavior.[10,11] One impressive example reported by Wei *et al.*, is $[Bu_4N]_3\{Dy[Mo_5O_{13}(OMe)_4(NO)]_2\}$, which exhibited a large energy barrier (U_{eff}) of 50 K.[10f] However, the documented Er-POM SMMs are very limited.[12] In 2008, Coronado *et al.* successfully synthesized the first example of Er-POMs exhibiting SMM behavior, $[ErW_{10}O_{36}]^{9-}$.[12a] Subsequently, they synthesized a series of Ln POMs and investigated their magnetic properties, $[Ln(W_5O_{18})_2]^{9-}$ (Ln = Tb, Dy, Ho, Er) and $[Ln(SiW_{11}O_{39})_2]^{13-}$ (Ln = Tb, Dy, Ho, Er, Tm, Yb), among which only the $[Er(W_5O_{18})_2]^{9-}$ derivative showed the SMM behavior

[a]*Henan Key Laboratory of Polyoxometalate Chemistry, College of Chemistry and Chemical Engineering, Henan University, Kaifeng, Henan 475004, P. R. China. E-mail: mpt@henu.edu.cn, jyniu@henu.edu.cn; Fax: +86-371-23886876*
[b]*Jiangsu Key Laboratory for NSLSCS, School of Physical Science and Technology, Nanjing Normal University, Nanjing 210023, China. E-mail: zhangyiquan@njnu.edu.cn*

†Electronic supplementary information (ESI) available: Crystallographic data, relevant structural tables, IR spectra, TGA curves, EDX spectra, and magnetic measurements (PDF). CCDC 1973436–1973438. For ESI and crystallographic data in CIF or other electronic format see DOI: 10.1039/D0DT01831G

above 2 K with an energy barrier of 55 K.[12c] In 2017, Jin *et al.* reported four mononuclear Ln-based germanomolybdates, $[Ln(GeMo_{11}O_{39})_2]^{13-}$ (Ln = Gd, Er, Dy, Tb); the magnetic results showed that $[Er(GeMo_{11}O_{39})_2]^{13-}$ and $[Dy(GeMo_{11}O_{39})_2]^{13-}$ exhibited slow magnetic relaxation behavior.[12d] Very recently, Kortz and co-worker addressed a new Er-POM-based SMM $[Er(\beta_2\text{-}GeW_{11}O_{39})(\alpha\text{-}GeW_{11}O_{39})]^{13-}$ with an effective barrier of 43.3 cm^{-1}.[12e] More importantly, polynuclear Er-based POM SMMs have not been reported until now, which arouses our keen interest and provides us with a great opportunity and challenge.

On the basis of the above theoretical and conceptual aspects, we synthesized a trinuclear Er-based POM $K_{20}Li_2[Er_3(\mu_3\text{-}OH)(H_2O)_8(AsW_9O_{33})(AsW_{10}O_{35}(DL\text{-}mal))]_2\cdot 51H_2O$ (mal = malate) (**1**), an isostructural Y-based analogue $K_{20}Li_2[Y_3(\mu_3\text{-}OH)(H_2O)_8(AsW_9O_{33})(AsW_{10}O_{35}(DL\text{-}mal))]_2\cdot 47H_2O$ (**2**), and a Er-doped analogue of **2**, $K_{20}Li_2[Er_{0.15}Y_{2.85}(\mu_3\text{-}OH)(H_2O)_8(AsW_9O_{33})(AsW_{10}O_{35}(DL\text{-}mal))]_2\cdot 44H_2O$ (**Er@2**) *via* simple one-pot reactions. Magnetic studies reveal that **1** exhibits field-induced SMM behavior with two magnetic relaxation processes, while **Er@2** shows slow magnetic relaxation at zero field.

Results and discussion

Crystal structure

X-ray single-crystal diffraction analysis reveals that the three compounds are isomorphous and crystallize in the monoclinic space group $P2_{1/n}$ (Table S1†). Therefore, only the structure of **1** is selected as an example to describe in detail.

Bond valence sum (BVS)[13] analysis for **1** indicates that the oxidation states of Er, As, and W centers are +3, +3 and +6, respectively (Table S2†). Compound **1** contains a centrosymmetric dimeric arsenotungstate polyanion $[Er_3(\mu_3\text{-}OH)(H_2O)_8(AsW_9O_{33})(AsW_{10}O_{35}(DL\text{-}mal))]_2^{22-}$ (Fig. 1a), which is composed of two organic–inorganic hybrid arsenotungstate subunits connected by malic ligands (Fig. 1b), $[Er_3(\mu_3\text{-}OH)(H_2O)_8(AsW_9O_{33})_2(WO_2(DL\text{-}mal))]^{11-}$. The asymmetric $[Er_3(\mu_3\text{-}OH)(H_2O)_8(AsW_9O_{33})_2(WO_2(DL\text{-}mal))]^{11-}$ unit consists of two $\{AsW_9O_{33}\}$ subunits that are nearly orientated at 180° with respect to each other. The space between them is occupied by the $\{Er_3\}$ segment and one $\{WO_2(DL\text{-}mal)\}$ unit,[14] which are linked by corner sharing to each other with the $\{AsW_9O_{33}\}$ subunit. More interestingly, the malic ligand is grafted onto the $[AsW_9O_{33}]^{9-}$ subunit *via* one carboxyl oxygen (O70) and

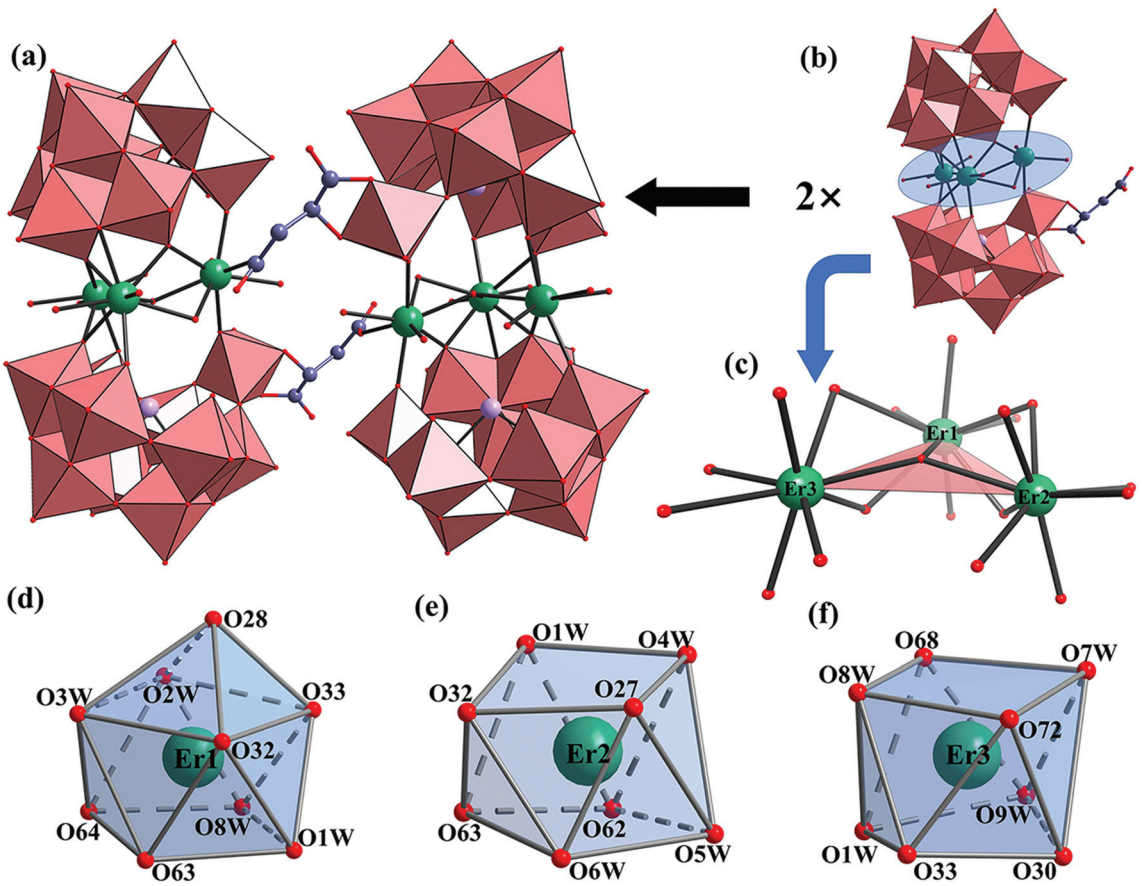

Fig. 1 Polyhedral/ball-and-stick representation of (a) $[Er_3(\mu_3\text{-}OH)(H_2O)_8(AsW_9O_{33})(AsW_{10}O_{35}(DL\text{-}mal))]_2^{22-}$, and (b) the subunit $[Er_3(\mu_3\text{-}OH)(H_2O)_8(AsW_9O_{33})_2(WO_2(DL\text{-}mal))]^{11-}$; (c) ball-and-stick representation of the triangular $\{Er_3\}$ cluster; (d) bicapped trigonal prismatic geometry of the Er1 cation; (e) square-antiprismatic geometry of the Er2 cation; (f) square-antiprismatic geometry of the Er3 cation; hydrogen atoms are omitted for clarity.

one hydroxyl oxygen (O69), while the carboxylic oxygen (O72) is attached to the $\{Er_3\}$ segment to produce the sandwiched $[Er_3(\mu_3\text{-}OH)(H_2O)_8(AsW_9O_{33})_2(WO_2(DL\text{-}mal))]^{11-}$ moiety, and a double-mal bridging tri-Er^{3+} segment sandwiched arsenotungstate dimer comes into being.

It is noteworthy that the Ln^{3+} ions usually exhibit variable higher coordination numbers: eight (dodecahedral, square antiprismatic, or bicapped trigonal prismatic) and nine (monocapped square antiprismatic or tricapped trigonal prismatic).[15] To evaluate the geometries and the extent of distortion from an ideal shape around the Er^{3+} ions in the $\{Er_3\}$ segment (Fig. 1c), we carried out continuous-shape measure analysis using the SHAPE 2.1 software.[16] The nine-coordinate Er1 center displays a spherical-capped square antiprism (C_{4v}) configuration (Tables S3 and S4†), and is coordinated by four terminal water molecules (O1 W, O2 W, O3 W and O8 W) [Er1–O(W): 2.310(9)–2.605(8) Å] (Fig. 1d), and five terminal oxygen atoms from the $[(AsW_9O_{33})_2]^{9-}$ fragment (O28, O32, O33, O63, and O64) [Er1–O: 2.349(5)–2.631(5) Å]. Both Er2 and Er3 cations show an eight-coordination square antiprism (D_{4d}) geometry (Tables S5 and S6†); Er2 is coordinated by four terminal oxygen atoms (O27, O32, O62 and O63) [Er2–O: 2.285(9)–2.484(9) Å], and four terminal water molecules (O1 W, O4 W, O5 W and O6 W) [Er2–O(W): 2.330(9)–2.412(10) Å] (Fig. 1f). Er3 is coordinated by four terminal water molecules (O1 W, O7 W, O8 W and O9 W) [Er3–O(W): 2.381(9)–2.452(8) Å], three terminal oxygen atoms (O30, O33, and O68) [Er3–O: 2.266(9)–2.305(8) Å] and one carboxylic oxygen atom (O72) [Er3–O72: 2.343(2) Å] from a malic ligand (Fig. 1e). These three Er^{3+} ions are combined together by four bridging oxygen atoms and one μ_3-oxo group (O1 W) presenting a nearly isosceles triangle. [Er1–Er2: 3.552(3), Er1–Er3: 3.586(4), Er2–Er3: 4.656(3), ∠Er1–Er3–Er2: 48.973(2)°, ∠Er1–Er2–Er3: 49.598(2)°, ∠Er2–Er1–Er3: 81.428(2)]° (Tables S7 and S8†). Unlike the reported tri-Ln sandwiched POMs, which showed a regular triangular Ln cluster with a CO_3^{2-} ion encapsulated in the center,[15b,c] the μ_3-bridging oxo group (O1 W) is noncoplanar with the three Er^{3+} ions plane, and the distance between the O1 W atom and the plane defined by the three Er^{3+} ions is 0.492(9) Å.

Magnetic measurements

The direct-current (dc) magnetic susceptibility for the crystalline sample of **1** was measured in the temperature range of 2–300 K under an applied field of 1000 Oe. At room temperature, the $\chi_M T$ value of **1** was 68.34 cm^3 K mol^{-1}, approximating to the expected value of six uncoupled Er^{3+} ions (68.85 cm^3 K mol^{-1}, $J = 15/2$, $g = 6/5$, $\chi_M T_{free\ ion} = 11.475$ cm^3 K mol^{-1}).[17] For **1** (Fig. 2a), the $\chi_M T$ value first stays essentially constant with only a little decrease upon cooling, before steeply decreasing to 42.80 cm^3 K mol^{-1} at 2.0 K, which is likely on account of the thermal depopulation of low lying crystal field (CF) states and/or antiferromagnetic coupling between the Er^{3+} ions in the triangular $\{Er_3\}$ cluster.[18] Besides, the magnetization was determined at 2.0, 3.0, and 5.0 K with the field dependence in the field range of 0–7 T (Fig. 2b). The result shows that the magnetization increases abruptly to 22.87$N\beta$ at 20 kOe. It increases

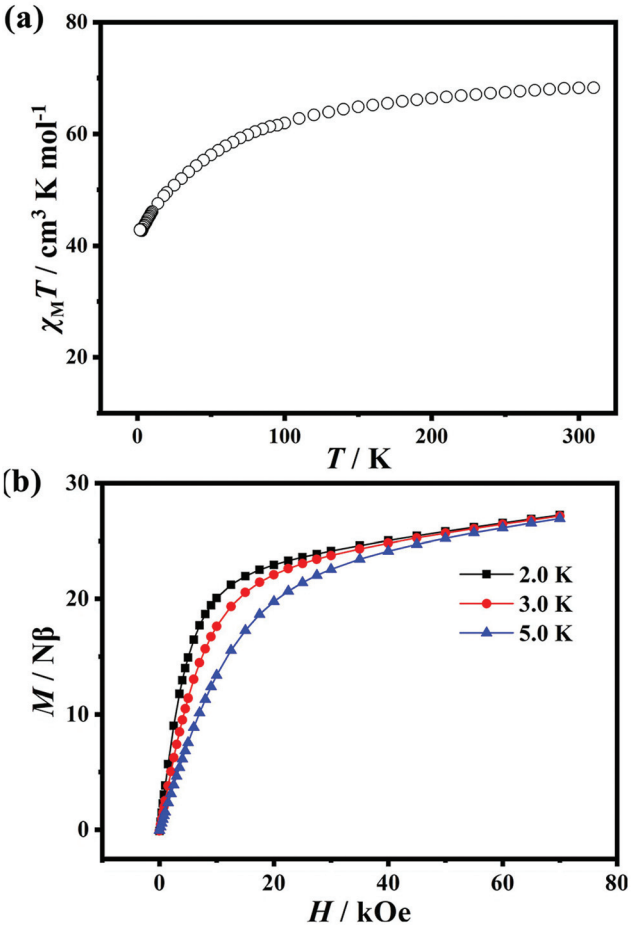

Fig. 2 (a) The temperature dependence of $\chi_M T$ measured under a 1000 Oe dc field for **1**. (b) The field dependence of magnetization at 2.0, 3.0, and 5.0 K.

slowly before reaching a maximum of 27.26$N\beta$ at 70 kOe without reaching the corresponding theoretical saturation value (54$N\beta$ for six Er^{3+} ions). Moreover, the non-superposed *M versus H*/*T* curves at different temperatures further indicate the presence of significant magnetic anisotropy and/or low-lying excited states.[19]

Alternating-current (ac) susceptibility measurements were conducted to explore the dynamic magnetic behavior of **1**. Variable-frequency magnetic susceptibility measurements reveal that for **1** under zero applied dc field (Fig. S4†), the maximum of χ_M'' increases with a drop in the temperature, which indicates the presence of QTM between the ground Kramers doublets for **1**.[20] In order to suppress the QTM effect, further ac susceptibility measurements were performed at 2.0 K under variable dc fields (500–5000 Oe) for **1**. Clear peaks were detected in the χ_M'' signals by the application of dc fields from 1500 Oe to 5000 Oe (Fig. S5†), which may be due to the inhibition of QTM. A 1500 Oe dc field was applied as the optimum field, which induces almost the slowest relaxation. For **1**, the strong χ_M'' signals with well-defined maxima (Fig. 3) suggest field-induced SMM behavior with two-step relaxation

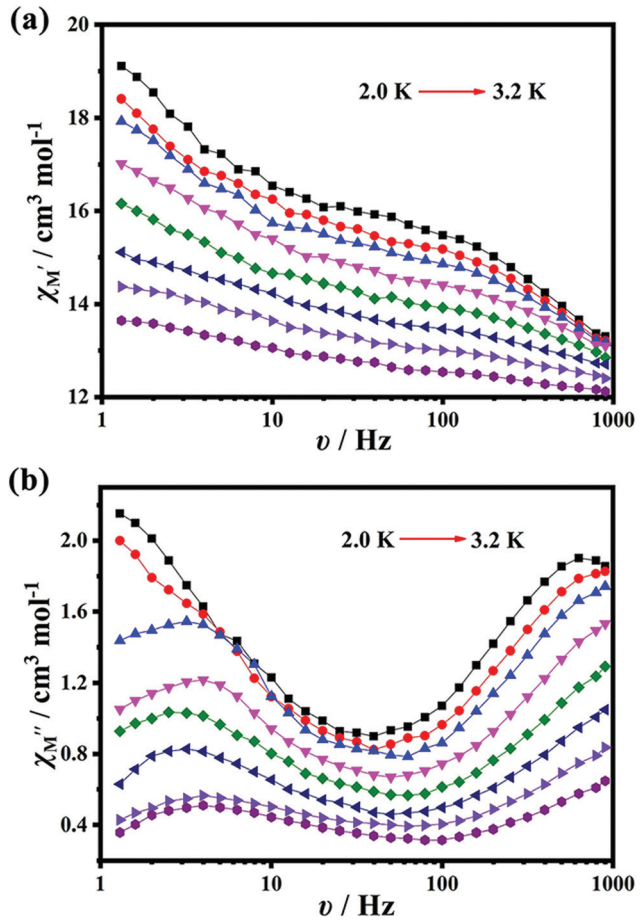

Fig. 3 Frequency dependence of χ_M' (a) and χ_M'' (b) under a 1500 dc field for **1**.

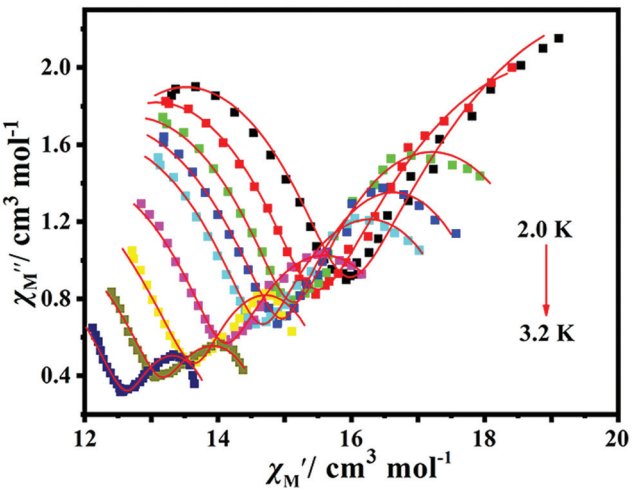

Fig. 4 Cole–Cole plot for **1** under an applied magnetic field of 1500 Oe at the indicated temperatures. The solid lines are fitting results by the generalized Debye model.

processes.[21] The results of χ_M'' susceptibilities show the appearance of two distinct groups of peaks above 2.0 K; the first full peaks were observed at lower frequencies and the second tails of peaks appeared at higher frequencies.

The Cole–Cole plot (Fig. 4) of **1** also shows two kinds of relaxation paths, respectively, corresponding to the fast relaxation (FR) phase and the slow relaxation (SR) phase.[22] The relaxation times for each process were extracted from the frequency-dependent data between 2.0 and 3.2 K on the basis of the sum of two modified Debye functions (Fig. S6–S13†). The relevant parameters are listed in Table S9.† The energy barriers for the two relaxation processes are obtained according to the Arrhenius law as 9.6(4) K ($\tau_0 = 2.1 \times 10^{-3}$ s) for the FR process and 9.1(3) K ($\tau_0 = 2.3 \times 10^{-6}$ s) for the SR process, respectively (Fig. S14†). The τ_0 value observed for the FR, which is far more than that expected for a SMM, strongly suggests that the quantum pathway of relaxation at very low temperature is not completely inhibited by the effects of the applied field (1500 Oe).[23]

In order to obtain further insight into the origin of the slow magnetic relaxation in **1**, the diluted sample **Er@2** was synthesized through crystallization with a diamagnetic and isostructural yttrium compound with an Er/Y molar ratio of 1 : 19 (Table S10†). Thus, the $\chi_M T$ value of the diluted **Er@2** sample was determined to be 5% of the dc susceptibility for the neat compound **1**. The $\chi_M T$ value of 3.42 cm^3 K mol^{-1} for **Er@2** is slightly smaller than the expected value (3.44 cm^3 K mol^{-1}, $J = 15/2$, $g = 6/5$) (Fig. 5a), which is mostly attributed to the splitting of the Russell–Saunders multiplet in a crystal field; thus, it cannot be equally populated even at room temperature, and this is also observed in some molecular magnets.[22] As the temperature is reduced from 300 K, the $\chi_M T$ values remain roughly constant in the range of 300–150 K for **Er@2**, before steeply decreasing to 2.28 cm^3 K mol^{-1} at 2.0 K, indicating the progressive depopulation of the excited Stark sublevels and/or antiferromagnetic exchange interactions. The field-dependent magnetization increases rapidly at low fields and then increases slightly to 1.32$N\beta$ at 7 T (Fig. 5b). The frequency-dependent χ_M' and χ_M'' signals of **Er@2** in ac magnetic susceptibility indicate a slow magnetic relaxation process under zero dc field (Fig. S15†), which indicates that the quantum tunneling can be partly but not totally suppressed as the intermolecular dipole–dipole interaction of the Er^{3+} ions is weakened upon dilution with diamagnetic ions.

In this case, the Cole–Cole plot was constructed between 1.8 and 4.0 K, with each temperature fitted by the generalized Debye model (Fig. S16†). A combination of the Orbach process and QTM ($\tau^{-1} = \tau_0^{-1} \exp[-U_{eff}/(kT)] + \tau_{QTM}^{-1}$) can fit the data of $\ln(\tau/s)$ *vs.* $1/T$ with $U_{eff} = 12.4(9)$ K, $\tau_0 = 4.7 \times 10^{-6}$ s and $\tau_{QTM} = 2.7 \times 10^{-4}$ s. The deviation from linearity can be attributed to a regime where both thermal and QTM mechanisms occur simultaneously (Fig. S17†).[24] In order to further suppress the QTM of **Er@2**, magnetic dynamics measurements were also performed under a 1500 Oe dc field. As shown in Fig. S18,† broad peaks of χ_M'' for **Er@2** are observed in the frequency-dependent ac susceptibilities. The relaxation process was

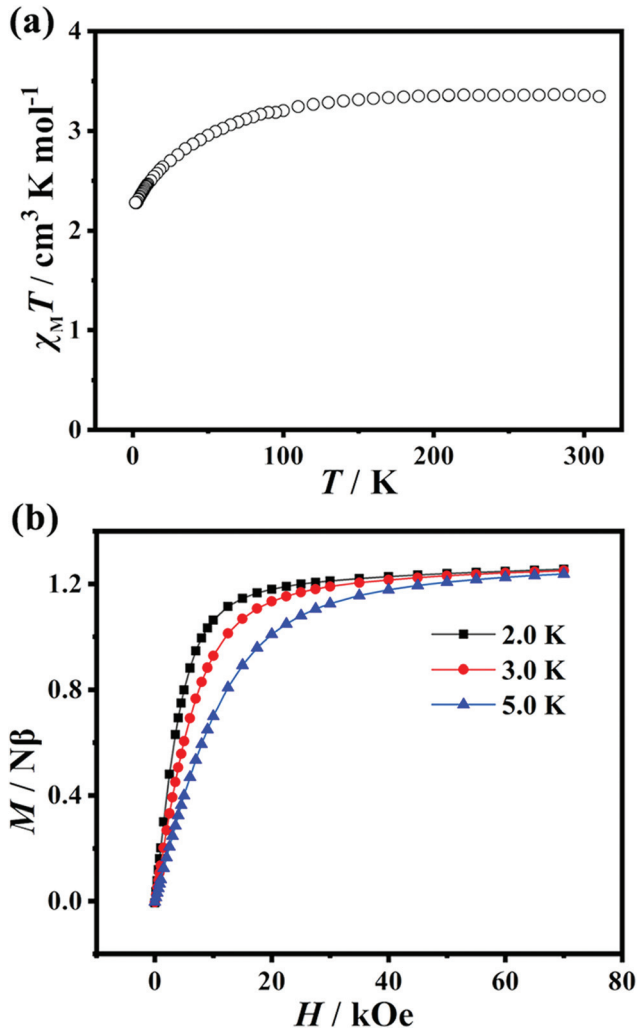

Fig. 5 (a) The temperature dependence of $\chi_M T$ measured under a 1000 Oe dc field for **Er@2**. (b) The field dependence of magnetization at 2.0, 3.0, and 5.0 K.

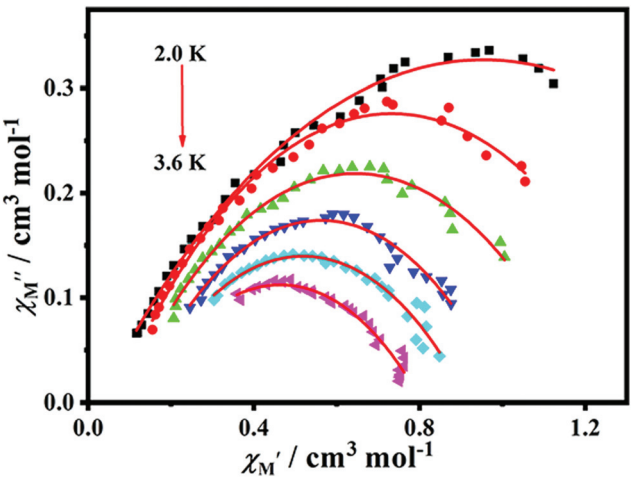

Fig. 6 Cole–Cole plot for **Er@2** under an applied magnetic field of 1500 Oe at the indicated temperatures.

further analyzed by the Arrhenius law, and the best fitting of the data of **Er@2** gave a U_{eff} value of 19.4(7) K and a τ_0 value of 3.3×10^{-6} (Fig. S19†). Compared with that of **1**, the Cole–Cole diagram of **Er@2** (Fig. 6 and Table S11†) clearly shows that the FR phase is effectively inhibited, demonstrating that the FR process in **1** originates from the intermolecular dipole–dipole interactions. It has been well established that the slow magnetic relaxation behavior of the polynuclear Ln^{3+}-based compound is primarily derived from the remarkable magnetic anisotropy and magnetic interactions.[25] Furthermore, the results of the experiments and related theoretical calculations in recent reports indicate that the applied dc field can compensate for these intramolecular magnetic interactions.[26] Considering that two-step magnetic relaxation processes in **1** are observed under a 1500 Oe applied dc field, we can presume that the SR process arises from intramolecular magnetic interactions and the FR process originates from the intermolecular dipole–dipole interactions.

Theoretical investigation

Complete-active-space self-consistent field (CASSCF) calculations on individual Er^{3+} fragments of compound **1** on the basis of the X-ray determined geometry have been carried out with MOLCAS 8.4 (ref. 27) and SINGLE_ANISO[28] programs (see ESI† for details). The energy levels (cm^{-1}), $\boldsymbol{g}$ (g_x, g_y, g_z) tensors and the predominant m_J values of the lowest eight Kramers doublets (KDs) of the individual Er^{3+} fragments for **1** are shown in Table S12.† The predominant m_J components for the lowest one or two KDs of the individual Er^{3+} fragments for **1** are shown in Table S13,† where the ground and first excited KDs are all mostly composed of several m_J states severelly. The magnetization blocking barriers of individual Er^{3+} fragments for **1** are shown in Fig. S20,† where the transversal magnetic moments in the ground KDs of **Er1**, **Er2**, and **Er3** are 0.26, 0.18 $\times 10^{-1}$, and 0.39 $\times 10^{-1} \mu_B$, respectively, therefore allowing fast QTM in their ground KDs. Although the magnetic anisotropies of **1** mainly originate from individual Er^{3+} fragments, the Er^{3+}–Er^{3+} interactions have a considerable influence on its slow magnetic relaxation processes. The program POLY_ANISO[28] was used to fit the magnetic susceptibility of the $\{Er_3\}$ fragment in **1** using the exchange parameters from Table 1.

All parameters from Table 1 were calculated with respect to the pseudospin $\tilde{S}_{Er} = 1/2$ on the Er^{3+} sites. For compound **1**,

Table 1 Fitted exchange coupling constants $\tilde{J}_{exch}$, the calculated dipole–dipole interactions $\tilde{J}_{dip}$ and $\tilde{J}_{total}$ between magnetic center ions in **1** (cm^{-1}). The intermolecular interaction zJ' of **1** was fitted to −0.16 cm^{-1}

	1		
	$\tilde{J}_{exch}$	$\tilde{J}_{dip}$	$\tilde{J}_{total}$
J_1	−3.5	1.3	−2.2
J_2	−5.4	−1.7	−7.1
J_3	−6.0	2.3	−3.7

the total coupling parameters $\tilde{J}_{total}$ (dipolar and exchange) Fig. S21† were included in fitting the magnetic susceptibility. The calculated and experimental $\chi_M T$ *versus* T plots of compound **1** are shown in Fig. S22,† where the fit is close to the experiment at low temperature, but they have some deviation at high temperature.[29] From Table 1, J_1, J_2, and J_3 in **1** within the Lines model[30] are all antiferromagnetic. Meanwhile, the exchange energies, the energy differences between each exchange doublet Δ_t and the main values of g_z for the lowest four exchange doublets of **1** are listed in Table S14,† where the g_z values of the ground exchange states for **1** are 29.318, which confirms that the Er^{3+}–Er^{3+} interactions for **1** are antiferromagnetic. The main magnetic axes on the Er^{3+} ions for **1** in their ground KDs are indicated in Fig. S23,† where the included angles between the magnetic axes on Er1, Er2, and Er3 are 94.51°, 83.06°, and 122.50°, respectively. *Ab initio* calculation results reveal that although the magnetic anisotropies of **1** mainly originate from individual Er^{3+} fragments, the Er^{3+}–Er^{3+} interactions have a considerable influence on their slow magnetic relaxation processes.

Conclusion

In summary, **1** and **Er@2** (diluted samples of **1** in their Y^{3+} analogues at a molar ratio of 1 : 19) have been successfully synthesized, structurally characterized and magnetic measurement carried out. One μ_3-oxygen caps the $\{Er_3\}$ triangle in **1**, and this is the first example of an infrequent μ_3-OH-capped $\{Er_3\}$ cluster containing POM-based SMM reported so far. Compound **1** shows two magnetic relaxation processes at a 1500 Oe dc field. Whereas, **Er@2** exhibits a field-induced single relaxation process, demonstrating that the fast relaxation process in **1** originates from the intermolecular dipole–dipole interactions. *Ab initio* calculation results manifest that although the magnetic anisotropies of **1** mainly originate from individual Er^{3+} fragments, the Er^{3+}–Er^{3+} interactions play a crucial role in its slow magnetic relaxation processes. This study further indicates that the magnetic-site dilution can be an effective approach for elucidating the nature of multiple relaxation processes of magnetization and further enhancing the magnetic performance of polynuclear Ln-POM SMMs.

Experimental

Synthesis of $K_{20}Li_2[Er_3(\mu_3\text{-}OH)(H_2O)_8(AsW_9O_{33})(AsW_{10}O_{35}(DL\text{-}mal))]_2\cdot 51H_2O$ (1)

The representative synthesis of **1** was performed as follows: a sample of $K_{14}[As_2W_{19}O_{67}(H_2O)]$ (1.32 g, 0.25 mmol) was added under stirring to a solution of 0.14 g DL-malic acid (1.04 mmol) and $ErCl_3\cdot 6H_2O$ (0.22 g, 0.60 mmol) in 20 mL of distilled water; ten minutes later, the pH of the solution was adjusted to approximately 6.5 with a 3.0 mol L^{-1} lithium hydroxide solution and then the mixture was heated to 60 °C for 1 h. After being cooled to room temperature, the clear solution was left to stand for crystallization. The light pink square crystals formed overnight. Yield: 0.71 g (29% based on $ErCl_3\cdot 6H_2O$). Elemental analysis (%) calcd for (**1**): C, 0.79; H, 0.65; Li, 0.11; K, 6.43; As, 2.47; Er, 8.26; W, 57.47. Found: C, 0.6; H, 0.986; Li, 0.08; K, 6.03; As, 2.23; Er, 8.01; W, 56.98. Selected IR (KBr, cm^{-1}): 3400 (br), 1627 (s), 1420 (w), 1369 (w), 1116 (w), 945 (s), 885 (s), 793 (s), 724 (s).

Synthesis of $K_{20}Li_2[Y_3(\mu_3\text{-}OH)(H_2O)_8(AsW_9O_{33})(AsW_{10}O_{35}(DL\text{-}mal))]_2\cdot 47H_2O$ (2)

A sample of $K_{14}[As_2W_{19}O_{67}(H_2O)]$ (1.32 g, 0.25 mmol) was added under stirring to a solution of 0.14 g DL-malic acid (1.04 mmol) and $YCl_3\cdot 6H_2O$ (0.18 g, 0.60 mmol) in 20 mL of distilled water; ten minutes later, the pH of the solution was adjusted to approximately 6.5 with a 3.0 mol L^{-1} lithium hydroxide solution and then the mixture was heated to 60 °C for 1 h. After being cooled to room temperature, the clear solution was made to stand for crystallization. The colorless square crystals formed overnight. Yield: 0.66 g (28% based on $YCl_3\cdot 6H_2O$) Elemental analysis (%) calcd for (**2**): C, 0.82; H, 0.67; Li, 0.12; K, 6.69; As, 2.56; Y, 4.56; W, 59.78. Found: C, 0.67; H, 0.71; Li, 0.08; K, 6.23; As, 2.50; Y, 4.36; W, 57.87. Selected IR (KBr, cm^{-1}): 3400 (br), 1627 (s), 1420 (w), 1364 (w), 1116 (w), 945 (s), 885 (s), 793 (s), 715 (s).

Synthesis of $K_{20}Li_2[Er_{0.15}Y_{2.85}(\mu_3\text{-}OH)(H_2O)_8(AsW_9O_{33})(AsW_{10}O_{35}$ (DL-mal))]$_2\cdot 44H_2O$ (Er@2)

(Er^{III} : Y^{III} = 1 : 19). A sample of $K_{14}[As_2W_{19}O_{67}(H_2O)]$ (1.32 g, 0.25 mmol) was added under stirring to a solution of 0.14 g DL-malic acid (1.04 mmol) and $ErCl_3\cdot 6H_2O$ (0.01 g, 0.03 mmol) and $YCl_3\cdot 6H_2O$ (0.17 g, 0.57 mmol) in 20 mL of distilled water; ten minutes later, the pH of the solution was adjusted to approximately 6.5 with a 3.0 mol L^{-1} lithium hydroxide solution and then the mixture was heated to 60 °C for 1 h. After being cooled to room temperature, the clear solution was left to stand for crystallization. The colorless square crystals formed overnight. Yield: 0.53 g. Elemental analysis (%) calcd for (**Er@2**): C, 0.85; H, 0.75; Li, 0.12; K, 6.89; As, 2.64; Er, 0.15; Y, 1.49; W, 61.58. Found: C, 0.65; H, 1.11; Li, 0.11; K, 6.65; As, 2.52; Er, 0.13; Y, 1.37; W, 60.59. Selected IR (KBr, cm^{-1}): 3400 (br), 1623 (s), 1424 (w), 1364 (w), 1116 (w), 945 (s), 890 (s), 793 (s), 720 (s).

Conflicts of interest

There are no conflicts to declare.

Acknowledgements

This work was financially supported by the National Nature Science Foundation of China (21573056 and 21973046), the Henan Province Science and Technology Attack Plan Project (182102210237) and the Major Project of Science and Technology, Education Department of Henan Province (20A150010).

Notes and references

1 (*a*) P. Yin, D. Li and T. Liu, *Chem. Soc. Rev.*, 2012, **41**, 7368–7383; (*b*) D. Li, P. Ma, J. Niu and J. Wang, *Coord. Chem. Rev.*, 2019, **392**, 49–80; (*c*) S. Reinoso, M. Giménez-Marqués, J. R. Galán-Mascarós, P. Vitoria and J. M. Gutiérrez-Zorrilla, *Angew. Chem., Int. Ed.*, 2010, **49**, 8384–8388.

2 (*a*) Z. Li, X. X. Li, T. Yang, Z. W. Cai and S. T. Zheng, *Angew. Chem., Int. Ed.*, 2017, **56**, 2664–2669; (*b*) Z. K. Zhu, Y. Y. Lin, H. Yu, X. X. Li and S. T. Zheng, *Angew. Chem.*, 2019, **58**, 16864–16868; (*c*) Y. Zhang, Y. Li, J. Pang, Y. Liu, P. Li, L. Chen and J. Zhao, *Inorg. Chem.*, 2019, **58**, 7078–7090; (*d*) Q. Han, Z. Li, X. M. Liang, Y. Ding and S. T. Zheng, *Inorg. Chem.*, 2019, **58**, 12534–12537.

3 (*a*) A. Nisar, Y. Lu, J. Zhuang and X. Wang, *Angew. Chem.*, 2011, **123**, 3245–3250; (*b*) H. Wu, B. Yan, H. Li, V. Singh, P. Ma, J. Niu and J. Wang, *Inorg. Chem.*, 2018, **57**, 7665–7675; (*c*) P. Ma, F. Hu, H. Wu, X. Liu, J. Wang and J. Niu, *J. Lumin.*, 2020, **217**, 116760.

4 (*a*) C. Ritchie, A. Ferguson, H. Nojiri, H. N. Miras, Y.-F. Song, D.-L. Long, E. Burkholder, M. Murrie, P. Kögerler and E. K. Brechin, *Angew. Chem.*, 2008, **120**, 5691–5694; (*b*) M. Ibrahim, V. Mereacre, N. Leblanc, W. Wernsdorfer, C. E. Anson and A. K. Powell, *Angew. Chem., Int. Ed.*, 2015, **54**, 15574–15578.

5 (*a*) J. He, Q. Han, J. Li, Z. Shi, X. Shi and J. Niu, *J. Catal.*, 2019, **376**, 161–167; (*b*) J. He, J. Li, Q. Han, C. Si, G. Niu, M. Li, J. Wang and J. Niu, *ACS Appl. Mater. Interfaces*, 2020, **12**, 2199–2206; (*c*) Z. Shi, J. Li, Q. Han, X. Shi, C. Si, G. Niu, P. Ma and M. Li, *Inorg. Chem.*, 2019, **58**, 12529–12533; (*d*) Y. Duan, J. M. Clemente-Juan, C. Giménez-Saiz and E. Coronado, *Inorg. Chem.*, 2016, **55**, 925–938; (*e*) T. Fukuda, N. Shigeyoshi, T. Yamamura and N. Ishikawa, *Inorg. Chem.*, 2014, **53**, 9080–9086; (*f*) J. Liu, Q. Han, L. Chen, J. Zhao, C. Streb and Y. Song, *Angew. Chem., Int. Ed.*, 2018, **57**, 8416–8420; (*g*) H. Wu, B. Yan, R. Liang, V. Singh, P. Ma, J. Wang and J. Niu, *Dalton Trans.*, 2020, **49**, 388–394.

6 (*a*) W. Wernsdorfer, N. Aliaga-Alcalde, D. N. Hendrickson and G. Christou, *Nature*, 2002, **416**, 406–409; (*b*) D. N. Woodruff, R. E. P. Winpenny and R. A. Layfield, *Chem. Rev.*, 2013, **113**, 5110–5148; (*c*) J. J. Baldoví, J. M. Clemente-Juan, E. Coronado, Y. Duan, A. Gaita-Ariño and C. Giménez-Saiz, *Inorg. Chem.*, 2014, **53**, 9976–9980; (*d*) Z. Zhu, M. Guo, X.-L. Li and J. Tang, *Coord. Chem. Rev.*, 2019, **378**, 350–364; (*e*) J. D. Rinehart and J. R. Long, *Chem. Sci.*, 2011, **2**, 2078–2085.

7 (*a*) D. Gatteschi, *Nat. Chem.*, 2011, **3**, 830; (*b*) R. L. Carlin, *Magnetochemistry*, Springer-Verlag, Berlin, 1986; (*c*) D. Gatteschi, R. Sessoli and J. Villain, *Molecular Nanomagnets*, Oxford University Press, Oxford, UK, 2006; (*d*) P. Zhang and J. Tang, *Lanthanide Single Molecular Magnets*, Springer-Verlag, Berlin, 2015; (*e*) J. D. Hilgar, M. G. Bernbeck and J. D. Rinehart, *J. Am. Chem. Soc.*, 2019, **141**, 1913–1917; (*f*) X. Zhang, D. Wang, J. Dou, S. Yan, X. Yao and J. Jiang, *Inorg. Chem.*, 2006, **45**, 10629–10635; (*g*) I. J. Hewitt, J. Tang, N. T. Madhu, C. E. Anson, Y. Lan, J. Luzon, M. Etienne, R. Sessoli and A. K. Powell, *Angew. Chem., Int. Ed.*, 2010, **49**, 6352–6356; (*h*) Y.-J. Ma, J.-X. Hu, S.-D. Han, J. Pan, J.-H. Li and G.-M. Wang, *J. Am. Chem. Soc.*, 2020, **142**, 2682–2689; (*i*) A. J. Brown, D. Pinkowicz, M. R. Saber and K. R. Dunbar, *Angew. Chem.*, 2015, **127**, 5962–5966; (*j*) K. Kumar, O. Stefanczyk, K. Nakabayashi, K. Imoto and S. Ohkoshi, *CrystEngComm*, 2019, **21**, 5882–5889.

8 (*a*) E. Coronado and C. J. Gómez-garcía, *Inorg. Chem.*, 1995, **17**, 255–281; (*b*) J. M. Clemente-Juan and E. Coronado, *Coord. Chem. Rev.*, 1999, **193–195**, 361–394; (*c*) J. M. Clemente-Juan, E. Coronado and A. Gaita-Ariño, *Chem. Soc. Rev.*, 2012, **41**, 7464–7478; (*d*) C. J. Calzado, J. M. Clemente-Juan, E. Coronado, A. Gaita-Arino and N. Suaud, *Inorg. Chem.*, 2008, **47**, 5889–5901; (*e*) A. Palii, B. Tsukerblat, S. Klokishner, K. R. Dunbar, J. M. Clemente-Juan and E. Coronado, *Chem. Soc. Rev.*, 2011, **40**, 3130–3156; (*f*) M. J. Clemente-Juan, E. Coronado, A. Gaita-Ariño, C. Giménez-Saiz, G. Chaboussant, H.-U. Güdel, R. Burriel and H. Mutka, *Chem. – Eur. J.*, 2002, **8**, 5701–5708.

9 (*a*) Y. Huo, R. Wan, P. Ma, J. Liu, Y. Chen, D. Li, J. Niu, J. Wang and M.-L. Tong, *Inorg. Chem.*, 2017, **56**, 12687–12691; (*b*) Y. Huo, Y.-C. Chen, S.-G. Wu, J.-H. Jia, W.-B. Chen, J.-L. Liu and M.-L. Tong, *Inorg. Chem.*, 2018, **57**, 6773–6777; (*c*) Y. Huo, Y.-C. Chen, S.-G. Wu, J.-L. Liu, J.-H. Jia, W.-B. Chen, B.-L. Wang, Y.-Q. Zhang and M.-L. Tong, *Inorg. Chem.*, 2019, **58**, 1301–1308; (*d*) M. Vonci and C. Boskovic, *Aust. J. Chem.*, 2014, **67**, 1542–1552.

10 (*a*) J. J. Baldoví, S. Cardona-Serra, J. M. Clemente-Juan, E. Coronado, A. Gaita-Ariño and A. Palii, *Inorg. Chem.*, 2012, **51**, 12565–12574; (*b*) M. Vonci, M. J. Giansiracusa, W. Van den Heuvel, R. W. Gable, B. Moubaraki, K. S. Murray, D. Yu, R. A. Mole, A. Soncini and C. Boskovic, *Inorg. Chem.*, 2017, **56**, 378–394; (*c*) X. Wang, Y. Liu, M. Jin, Y. Wu, L. Chen and J.-W. Zhao, *Cryst. Growth Des.*, 2017, **17**, 5295–5308; (*d*) J. J. Baldoví, Y. Duan, C. Bustos, S. Cardona-Serra, P. Gouzerh, R. Villanneau, G. Gontard, J. M. Clemente-Juan, A. Gaita-Ariño and C. Giménez-Saiz, *Dalton Trans.*, 2016, **45**, 16653–16660; (*e*) Z. Jin, J. Bai, T. Wei, F. Li, C. Song, X. Luo and L. Xu, *New J. Chem.*, 2017, **41**, 13490–13494; (*f*) S. She, C. Gao, K. Chen, A. Bayaguud, Y. Huang, B.-W. Wang, S. Gao and Y. Wei, *Inorg. Chem.*, 2018, **57**, 963–969.

11 (*a*) P. Ma, F. Hu, R. Wan, Y. Huo, D. Zhang, J. Niu and J. Wang, *J. Mater. Chem. C*, 2016, **4**, 5424–5433; (*b*) P. Ma, F. Hu, Y. Huo, D. Zhang, C. Zhang, J. Niu and J. Wang, *Cryst. Growth Des.*, 2017, **17**, 1947–1956; (*c*) S. Cardona-Serra, J. M. Clemente-Juan, E. Coronado, A. Gaita-Ariño, A. Camón, M. Evangelisti, F. Luis, M. J. Martínez-Pérez and J. Sesé, *J. Am. Chem. Soc.*, 2012, **134**, 14982–14990; (*d*) S.-Y. Lin, L. Zhao, Y.-N. Guo, P. Zhang, Y. Guo and J. Tang, *Inorg. Chem.*, 2012, **51**, 10522–10528; (*e*) C. Ritchie, M. Speldrich, R. W. Gable, L. Sorace, P. Kögerler and C. Boskovic, *Inorg. Chem.*, 2011, **50**, 7004–7014.

12 (*a*) M. A. AlDamen, J. M. Clemente-Juan, E. Coronado, C. Martí-Gastaldo and A. Gaita-Ariño, *J. Am. Chem. Soc.*, 2008, **130**, 8874–8875; (*b*) F. Luis, M. J. Martínez-Pérez, O. Montero, E. Coronado, S. Cardona-Serra, C. Martí-Gastaldo, J. M. Clemente-Juan, J. Sesé, D. Drung and T. Schurig, *Phys. Rev. B: Condens. Matter Mater. Phys.*, 2010, **82**, 060403; (*c*) M. A. AlDamen, S. Cardona-Serra, J. M. Clemente-Juan, E. Coronado, A. Gaita-Ariño, C. Martí-Gastaldo, F. Luis and O. Montero, *Inorg. Chem.*, 2009, **48**, 3467–3479; (*d*) Z. Jin, J. Bai, T. Wei, F. Li, C. Song, X. Luo and L. Xu, *New J. Chem.*, 2017, **41**, 13490–13494; (*e*) A. S. Mougharbel, S. Bhattacharya, B. S. Bassil, A. Rubab, J. van Leusen, P. Kogerler, J. Wojciechowski and U. Kortz, *Inorg. Chem.*, 2020, **59**, 4340–4348.

13 W. Liu and H. H. Thorp, *Inorg. Chem.*, 1993, **32**, 4102–4105.

14 C. Ritchie, V. Baslon, E. G. Moore, C. Reber and C. Boskovic, *Inorg. Chem.*, 2012, **51**, 1142–1151.

15 (*a*) L. Helm and A. E. Merbach, *Coord. Chem. Rev.*, 1999, **187**, 151–181; (*b*) X. Fang, T. M. Anderson, W. A. Neiwert and C. L. Hill, *Inorg. Chem.*, 2003, **42**, 8600–8602; (*c*) R. Khoshnavazi, F. Nicolò, H. Amiri Rudbari, E. Naseri and A. Aminipour, *J. Coord. Chem.*, 2013, **66**, 1374–1383.

16 M. Llunell, D. Casanova, J. Cirera, J. M. Bofill, P. Alemany, S. Alvarez, M. Pinsky and D. Avnir, *SHAPE V2.1*, Universitat de Barcelona, 2013.

17 J.-P. Costes, J. M. Clemente-Juan, F. Dahan, F. Nicodème and M. Verelst, *Angew. Chem.*, 2002, **114**, 333–335.

18 N. Ishikawa, M. Sugita, T. Ishikawa, S. Koshihara and Y. Kaizu, *J. Am. Chem. Soc.*, 2003, **125**, 8694–8695.

19 (*a*) J. Jia, Y. Niu, P. Zhang, D. Zhang, P. Ma, C. Zhang, J. Niu and J. Wang, *Inorg. Chem.*, 2017, **56**, 10131–10134; (*b*) Y.-J. Ma, J.-X. Hu, S.-D. Han, J. Pan, J.-H. Li and G.-M. Wang, *Chem. Commun.*, 2019, **55**, 5631–5634.

20 (*a*) S. Zhang, H. Ke, X. Liu, Q. Wei, G. Xie and S. Chen, *Chem. Commun.*, 2015, **51**, 15188–15191; (*b*) J.-L. Liu, K. Yuan, J.-D. Leng, L. Ungur, W. Wernsdorfer, F.-S. Guo, L. F. Chibotaru and M.-L. Tong, *Inorg. Chem.*, 2012, **51**, 8538–8544.

21 L. Sun, S. Zhang, Z. Jiang, Q. Yang, S. Chen, Y. Zhang, W. Wang, Q. Wei and G. Xie, *Dalton Trans.*, 2017, **46**, 11159–11165.

22 (*a*) P. Zhang, L. Zhang, C. Wang, S. Xue, S.-Y. Lin and J. Tang, *J. Am. Chem. Soc.*, 2014, **136**, 4484–4487; (*b*) L. Sun, S. Zhang, C. Qiao, S. Chen, B. Yin, W. Wang, Q. Wei, G. Xie and S. Gao, *Inorg. Chem.*, 2016, **55**, 10587–10596.

23 (*a*) L. Li, S. Liu, H. Li, W. Shi and P. Cheng, *Chem. Commun.*, 2015, **51**, 10933–10936; (*b*) J. Ruiz, A. J. Mota, A. Rodríguez-Diéguez, S. Titos, J. M. Herrera, E. Ruiz, E. Cremades, J. P. Costes and E. Colacio, *Chem. Commun.*, 2012, **48**, 7916–7918.

24 (*a*) S. T. Liddle and J. Slageren, *Chem. Soc. Rev.*, 2015, **44**, 6655–6669; (*b*) C. M. Dickie and M. Nippe, *Inorg. Chem. Front.*, 2016, **3**, 97–103; (*c*) A. V. Funes, L. Carrella, E. Rentschler and P. Alborés, *Dalton Trans.*, 2014, **43**, 2361–2364.

25 (*a*) X. Yi, K. Bernot, F. Pointillart, G. Poneti, G. Calvez, C. Daiguebonne, O. Guillou and R. Sessoli, *Chem. – Eur. J.*, 2012, **18**, 11379–11387; (*b*) J. Tang, I. Hewitt, N. T. Madhu, G. Chastanet, W. Wernsdorfer, C. E. Anson, C. B. Benelli, R. Sessoli and A. K. Powell, *Angew. Chem., Int. Ed.*, 2006, **45**, 1729–1733; (*c*) Y.-N. Guo, G.-F. Xu, W. Wernsdorfer, L. Ungur, Y. Guo, J. Tang, H.-J. Zhang, L. F. Chibotaru and A. K. Powell, *J. Am. Chem. Soc.*, 2011, **133**, 11948–11951; (*d*) J. Xiong, H.-Y. Ding, Y.-S. Meng, C. Gao, X.-J. Zhang, Z.-S. Meng, Y.-Q. Zhang, W. Shi, B.-W. Wang and S. Gao, *Chem. Sci.*, 2017, **8**, 1288–1294; (*e*) X.-Q. Ji, F. Ma, J. Xiong, J. Yang, H.-L. Sun, Y.-Q. Zhang and S. Gao, *Inorg. Chem. Front.*, 2019, **6**, 786–790.

26 (*a*) E. M. Fatila, M. Rouzières, M. C. Jennings, A. J. Lough, R. Clérac and K. E. Preuss, *J. Am. Chem. Soc.*, 2013, **135**, 9596–9599; (*b*) L. Zhang, J. Jung, P. Zhang, M. Guo, L. Zhao, J. Tang and B. L. Guennic, *Chem. – Eur. J.*, 2016, **22**, 1392–1398; (*c*) I. F. DíazOrtega, J. M. Herrera, D. Aravena, E. Ruiz, T. Gupta, G. Rajaraman, H. Nojiri and E. Colacio, *Inorg. Chem.*, 2018, **57**, 6362–6375; (*d*) Y. Fang, X.-Q. Ji, J. Xiong, G. Li, F. Ma, H.-L. Sun, Y.-Q. Zhang and S. Gao, *Dalton Trans.*, 2018, **47**, 11636–11644; (*e*) S. Zhang, W. Mo, B. Yin, G. Zhang, D. Yang, X. Lü and S. Chen, *Dalton Trans.*, 2018, **47**, 12393–12405.

27 F. Aquilante, J. Autschbach, R. K. Carlson, L. F. Chibotaru, M. G. Delcey, L. De Vico, I. F. Galván, N. Ferré, L. M. Frutos, L. Gagliardi, M. Garavelli, A. Giussani, C. E. Hoyer, G. Li Manni, H. Lischka, D. Ma, P. Å. Malmqvist, T. Müller, A. Nenov, M. Olivucci, T. B. Pedersen, D. Peng, F. Plasser, B. Pritchard, M. Reiher, I. Rivalta, I. Schapiro, J. Segarra-Martí, M. Stenrup, D. G. Truhlar, L. Ungur, A. Valentini, S. Vancoillie, V. Veryazov, V. P. Vysotskiy, O. Weingart, F. Zapata and R. Lindh, MOLCAS 8: New Capabilities for Multiconfigurational Quantum Chemical Calculations across the Periodic Table, *J. Comput. Chem.*, 2016, **37**, 506–541.

28 (*a*) L. F. Chibotaru, L. Ungur and A. Soncini, *Angew. Chem., Int. Ed.*, 2008, **47**, 4126–4129; (*b*) L. Ungur, W. Van den Heuvel and L. F. Chibotaru, *New J. Chem.*, 2009, **33**, 1224–1230; (*c*) L. F. Chibotaru, L. Ungur, C. Aronica, H. Elmoll, G. Pilet and D. Luneau, *J. Am. Chem. Soc.*, 2008, **130**, 12445–12455.

29 S. K. Langley, D. P. Wielechowski, V. Vieru, N. F. Chilton, B. Moubaraki, B. F. Abrahams, L. F. Chibotaru and K. S. Murray, *Angew. Chem., Int. Ed.*, 2013, **52**, 12014–12019.

30 M. E. Lines, *J. Chem. Phys.*, 1971, **55**, 2977.